Available online at www.sciencedirect.com
ScienceDirect
Trans. Nonferrous Met. Soc. China 34(2024) 3707−3720
Transactions of Nonferrous Metals Society of China
www.tnmsc.cn

Mechanism of lime decomposing Al_2O_3-containing fayalite melt

Hui-chuan REN[1], Xiao-bo MIN[1,2,3], Yong KE[1,2,3], Long-gong XIA[1], Yun-yan WANG[1,2,3], Cong PENG[1,2,3], Yun LI[1,2,3], Rong-he TAN[4], Chuan-fu ZHANG[1,2,3]

1. School of Metallurgy and Environment, Central South University, Changsha 410083, China;
2. State Key Laboratory of Advanced Metallurgy for Non-ferrous Metals, Changsha 410083, China;
3. Chinese National Engineering Research Center for Control & Treatment of Heavy Metal Pollution, Changsha 410083, China;
4. CINF Engineering Corporation Limited, Changsha 410001, China

Received 26 December 2023; accepted 20 June 2024

Abstract: A method to upgrade the iron grade in copper slag was proposed using lime to decompose Al_2O_3-containing fayalite melt (AFMT). Thermodynamic calculations indicated that adjusting the CaO/AFMT ratio can yield a residual melt with a FeO concentration of 75−88 wt.% and produce Ca_2SiO_4. In-situ observations suggested that the reaction was impeded in some way. Quenching experiments revealed that the initial reaction products consisted of calcium ferrite compounds and FeO−CaO melt. At the FeO−CaO melt/AFMT interface, Ca_2SiO_4 particles precipitated, forming a dense Ca_2SiO_4 film that significantly impeded mass transfer. Although trace amounts of Al_2O_3 in AFMT temporarily enhanced mass transfer, they were insufficient to overcome this retardation effect. The decomposition reaction was far from achieving equilibrium, demonstrating a self-retardation effect. Measures must be implemented to eliminate this self-retardation effect and enhance the efficiency of reaction kinetics.

Key words: lime; Al_2O_3-containing fayalite melt; Ca_2SiO_4 film; self-retardation; mass transfer

1 Introduction

As environmental concerns rise globally, several nations have established timelines for phasing out the sale of fossil fuel vehicles [1−3]. The shift toward electric vehicles represents an irreversible trend [4−6]. Copper, noted for its high electrical and thermal conductivity, along with its ductility, is becoming increasingly important in power conversion and transmission within the new energy sector, thereby increasing copper demand [7−9]. Model projections suggest that the global stock of copper in use will surge from 380×10^6 t in 2015 to 880×10^6 t by 2050 [10]. A predominant by-product of copper smelting is copper slag, with production rates of 2.2 t of slag per ton of electrolytic copper [11,12]. Typically, the iron content of copper slag is about 40 wt.% [13]. It is estimated that around 80% of copper slag globally is discarded, which not only squanders limited metal iron resources but also severely impacts the ecological environment [14,15]. Therefore, enhancing the resource utilization efficiency of copper slag and promoting green, low-carbon development are imperative, with a strong emphasis on environmental protection.

Copper slag is also referred to as fayalite slag [16,17], named after its primary constituents found within the fayalite (Fe_2SiO_4) phase field in the FeO−CaO−SiO_2 diagram [18]. Besides fayalite, copper slag contains minor quantities of

Corresponding author: Yong KE, Tel: +86-13548696693, E-mail: keyong000ke@csu.edu.cn
DOI: 10.1016/S1003-6326(24)66635-5

gangue materials such as CaO and Al_2O_3 [19]. Although copper slag has been partially utilized in production of abrasive and cutting tools due to high hardness of fayalite [20,21], the volume employed in these applications remains minimal. The predominant approach to the copper slag management has been through pyrometallurgical methods, favored for their established technology and substantial processing capacity. The Fe concentration in copper slag [22] is considerably lower than that in the sintered ore or pellets (55−65 wt.%) [23,24]. Utilizing copper slag directly in blast furnaces or alternative metallurgical processes is inefficient due to the high SiO_2 content, which necessitates additional flux and coke [25,26]. Therefore, enhancing the iron concentration in copper slag prior to its use in metallurgical processes is essential [27]. The decomposition of fayalite is central to this objective.

Molten oxidation technology [28,29] has been employed to enrich iron resources from molten copper slag. Under rich oxygen conditions, Fe_2SiO_4 melt can be oxidized, decomposing into Fe_3O_4 and SiO_2 [30]. However, the continuous formation of Fe_3O_4 increases the viscosity, thus impeding oxygen transfer. To simplify operational complexity, it is advantageous to decompose the fayalite melt without oxidation, thereby enriching the iron content in the form of FeO. Ternary FeO−CaO−SiO_2 phase diagram [31], widely used in pyrometallurgy and mineral processing, supports this process. By adding CaO to the fayalite melt until the composition reaches the primary phase field of Ca_2SiO_4, Ca_2SiO_4 precipitates, thus increasing the FeO content of the residual melt. This approach, which uses lime to decompose the fayalite melt and increase the iron grade of copper slag, contrasts sharply with slag control methods in the hot metal dephosphorization process. Accordingly, studies on the formation of hot metal dephosphorization slag [32−36] can provide guidance to a certain extent. However, it is crucial to recognize that varying experimental conditions, characterization methods, and research focuses can lead to diverse results and potentially inconsistent conclusions. Additionally, the effects of Al_2O_3 are not uniform [37,38], necessitating further investigation into the mechanisms by which lime decomposes Al_2O_3-containing fayalite melt (AFMT) to inform future research.

In this study, a high-temperature confocal scanning laser microscope (CSLM) was utilized to observe the in-situ reaction of solid CaO decomposing AFMT. Experimental designs aimed at understanding the reaction mechanism revealed that the formation of a compact Ca_2SiO_4 film significantly hinders mass transfer, effectively terminating the reaction. This led to the proposal of a self-retardation mechanism for the reaction of CaO decomposing AFMT.

2 Experimental

2.1 Chemical reagents

Iron powder, Fe_3O_4, SiO_2, and Al_2O_3 used in this study had a purity of 99.9 wt.% and were purchased from Shanghai Aladdin Chemical Reagent Co., Ltd., China. Argon gas, with a purity of 99.999 vol.%, was supplied by Hunan Chitai Gases Co., Ltd., China.

2.2 Experimental procedure

The experimental procedure involved the preparation of Al_2O_3-containing fayalite, in-situ observation of lime decomposing AFMT, and lime decomposing AFMT, as illustrated in Fig. 1.

(1) Preparation of materials

A total of 98 g of iron powder, Fe_3O_4, and SiO_2 were weighed in a molar ratio of 1∶1∶2 and mixed with 2 g of Al_2O_3. This mixture was placed in an iron crucible and introduced into a muffle furnace supplied with argon at a flow rate of 300 mL/min. The furnace temperature was programmed to reach 1300 °C and maintained for 6 h. Afterward, the synthesized material was quenched in an ice-water bath, dried at 105 °C for 1 h, and ground for 2 min using a vibrator. The resulting X-ray diffraction pattern is presented in Fig. 2. Solid CaO, with a density of 3.28 g/cm^3, was synthesized following the method described in Ref. [36].

(2) In-situ observation of lime decomposing AFMT

The experimental setup, including the CSLM model SVF17SP-VL2000DX (Japan), and the temperature control profile are depicted in Fig. 1(a). Detailed descriptions of the CSLM are provided in previous studies [39,40]. A 20 mg particle of CaO was placed atop 30 mg of Al_2O_3-containing fayalite powder in a platinum crucible. Following the temperature control profile shown in Fig. 1(b), the

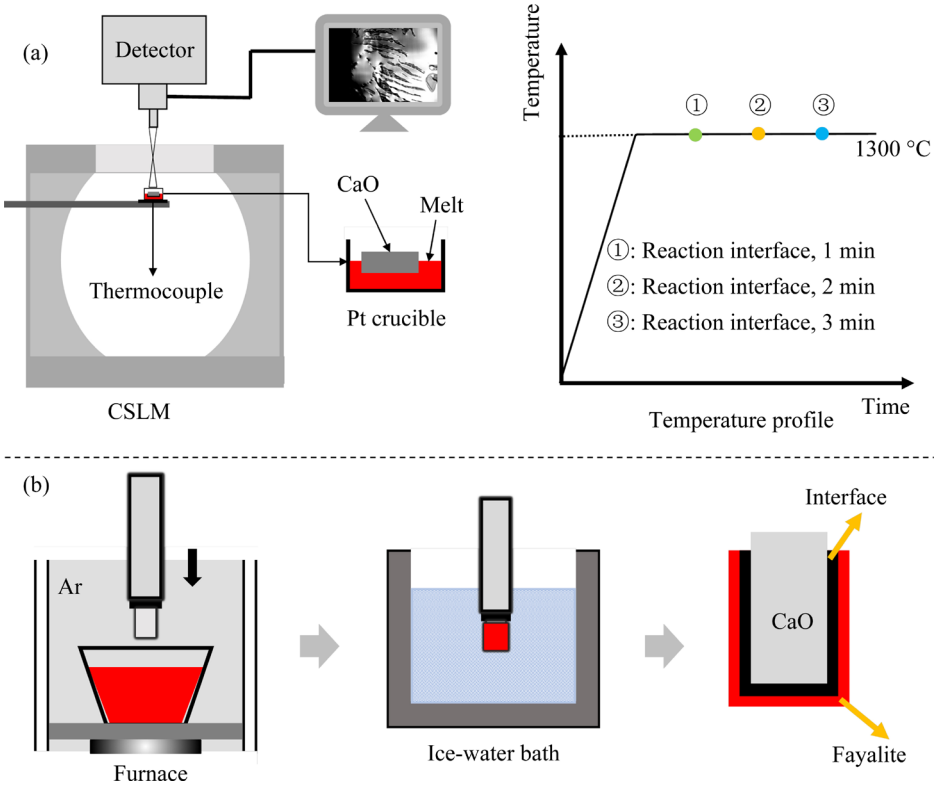

Fig. 1 Schematic diagrams showing in-situ observation of lime decomposing AFMT (a) and experimental procedure of lime decomposing AFMT (b)

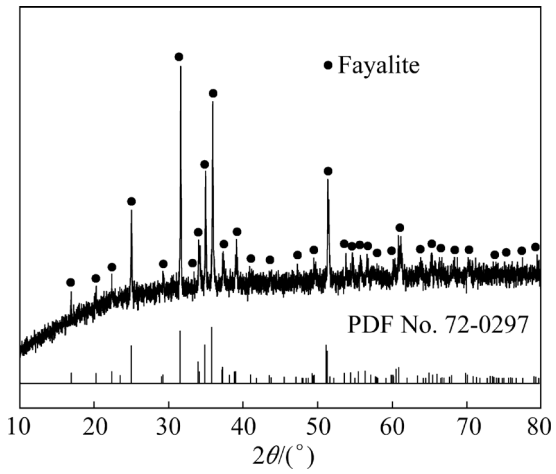

Fig. 2 XRD pattern of quenched AFMT

sample was heated to 1300 °C and maintained for 1, 2, and 3 min. Images were captured at the solid CaO/AFMT interface, denoted by markers ①, ②, and ③.

(3) Lime decomposing AFMT

A 30 mL iron crucible containing 15 g of Al_2O_3-containing fayalite powder was positioned in a muffle furnace, as shown in Fig. 1(b). A height-adjustable alumina tube was inserted into the muffle furnace, with its bottom bonded with a cylindrical CaO, positioned 10 mm above the iron crucible. Argon was introduced into the muffle furnace at a flow rate of 600 mL/min. The temperature was set to 1220 °C and maintained for 20 min. The alumina tube was lowered and quickly withdrawn once the cylindrical CaO was immersed in the melt; then, it was quenched with a total process time of 1 s (which was considered the reaction time). For subsequent trials, the tube was retracted to the initial position and held for 0, 9, and 29 s before quenching. These trials, conducted at 1300 °C, had corresponding reaction time of 1, 10, and 30 s.

2.3 Characterization methods

The synthesized sample was analyzed using an X-ray powder diffractometer (PANalytical Empyrean−2). The interfaces of the quenched samples were examined with electron probe X-ray microanalysis (EPMA, JEOL JXA−8530F). The pseudo-ternary phase diagram for the $FeO−CaO−SiO_2$ system containing 2.0 wt.% Al_2O_3 system was obtained using the thermochemical software FactSage (Version 8.2) [41], utilizing the oxide database.

3 Thermodynamic analysis

The equilibrium composition of the chemical system was assessed through thermodynamic calculations. Figure 3 presents the pseudo-ternary phase diagram for the FeO−CaO−SiO_2 system, incorporating Al_2O_3, at 1300 °C. The diagram includes Al_2O_3 concentrations of 0−2 wt.%, which corresponds to 0−3.8 wt.% Al_2O_3 within the AFMT. This range encompasses the typical Al_2O_3 levels found in most copper slags. By adjusting the composition to remain within the Ca_2SiO_4 primary phase field, the equilibrium products are solid Ca_2SiO_4 and a residual melt that adheres to the liquidus curve. In the shadowed region of the diagram, the FeO concentration in the residual melt spans 75−88 wt.%, which corresponds to an iron concentration of 58.3−68.4 wt.%. This residual melt has a higher concentration of the alkaline gangue component CaO compared to the acidic gangue components SiO_2 and Al_2O_3. Although traces of Al_2O_3 may marginally decrease the concentration of iron oxide, they do not significantly impair the melt's potential as a valuable iron-rich resource.

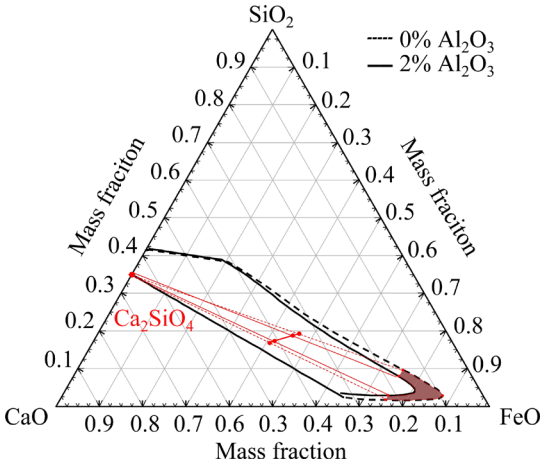

Fig. 3 Phase diagram of pseudo-ternary FeO−CaO−SiO_2 system under conditions of Al_2O_3/(SiO_2+FeO+CaO+Al_2O_3) mass ratios of 0 and 0.02, 1300 °C, and 1.013×10^5 Pa

4 Results and discussion

4.1 In-situ observation

Figures 4(a−c) show the in-situ observation of the solid CaO/AFMT reaction interface held at 1300 °C for durations of 1, 2, and 3 min, respectively. The interface consists of coexisting solid and molten phases. Notably, the interface appears largely unchanged from 1 to 3 min, with the formation of only small solid particles in an isolated area to the right of the interface. During this period, the chemical interaction between solid CaO and AFMT appears to reach a near standstill.

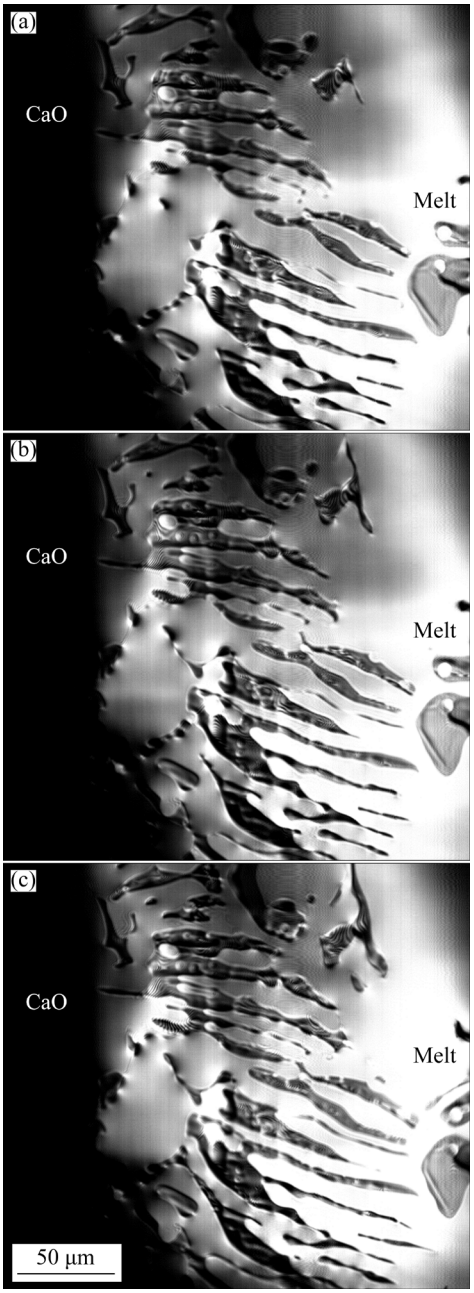

Fig. 4 CSLM images of reaction interface at 1300 °C for 1 min (a), 2 min (b), and 3 min (c)

The composition of reactants for these observations was maintained within the Ca_2SiO_4 primary phase field of the FeO−CaO−SiO_2 phase diagram. Based on thermodynamic principles, the interface should have continued to evolve until the system transformed into a mixture of melt and solid

particles.

Considering the residual melt saturated with FeO and assuming that AFMT is devoid of Al_2O_3, the reaction equation for lime decomposing AFMT can be expressed as

$$Fe_2SiO_4(l)+2CaO(s)=Ca_2SiO_4(s)+2FeO$$

The equilibrium constant for this reaction at 1300 °C, as calculated using FactSage 8.2, is 1.37×10^4.

This discrepancy between the observed stagnation of the reaction interface and the substantial equilibrium constant suggests a need for a new perspective to comprehensively understand and elucidate the reaction mechanism.

4.2 CaO decomposing AFMT

4.2.1 Phase assemblages

EPMA measurement was conducted on the cross-sections of the polished samples, as depicted in Fig. 5. Specific measurement points were selected to quantify the chemical composition and identify the phases; the results are presented in Table 1. Spots 1 and 2 in Fig. 5(a) correspond to wustite and residues precipitated from AFMT during quenching, respectively. Typically, the formation of dendritic wustite results from nonuniform heat transfer during quenching and compositional segregation during the solidification of AFMT (Spot 3). Additionally, other phases such as calcium ferrite compounds, FeO−CaO melt, Ca_2SiO_4, and Ca_3SiO_5 are observed in the back-scattered EPMA images and will be discussed in detail later.

4.2.2 Effect of temperature

At 1220 °C, observations at the reaction interface revealed the presence of calcium ferrite compounds and FeO−CaO melt. At 1300 °C with a reaction time of 1 s, a product layer composed of Ca_2SiO_4 particles was also detected.

The initial reaction products of CaO decomposing AFMT included calcium ferrite compounds and FeO−CaO melt, as identified in Fig. 5(a) and corroborated by the data in Table 1. The cylindrical CaO and adhering AFMT were relatively stationary, and the chemical reactions occurred via ionic diffusion [42]. Specifically, Ca^{2+} from cylindrical CaO and Fe^{2+} from AFMT underwent diffusion. The SiO_4^{4-}, which dissolved Al_2O_3, diffused in the same direction as Fe^{2+}. Consequently, Ca concentrations decreased from the cylindrical CaO to the AFMT, while Fe and Si concentrations showed the opposite trend, as illustrated in Fig. 6. SiO_4^{4-}, having a larger ionic

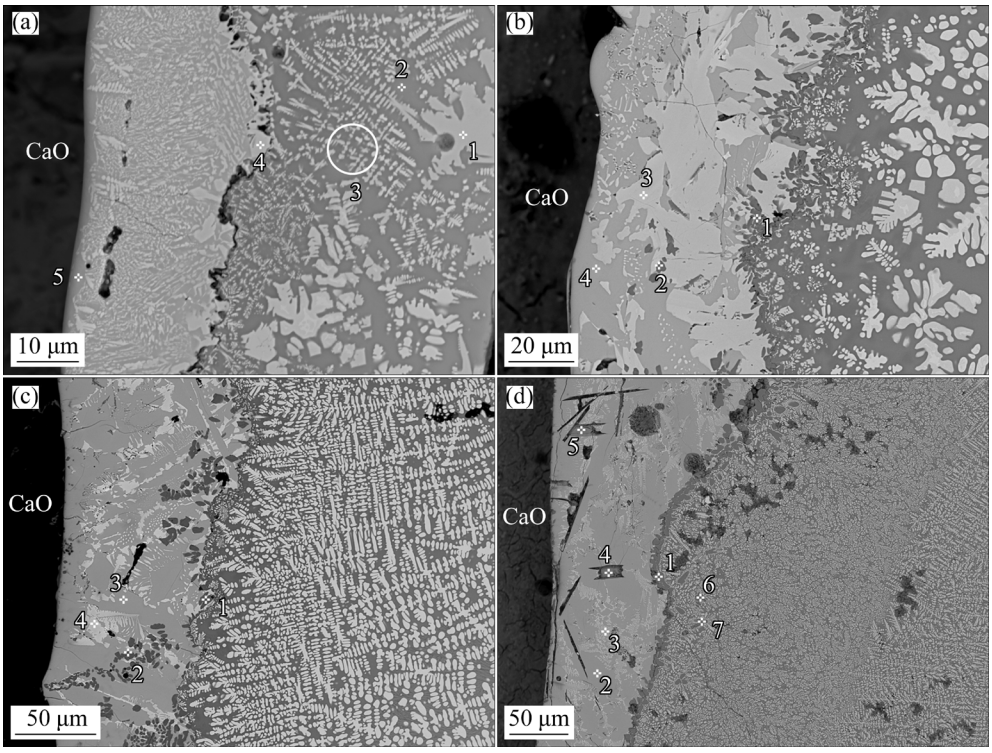

Fig. 5 Backscattered images of quenched samples at 1220 °C for 1 s (a), and at 1300 °C for 1 s (b), 10 s (c) and 30 s (d)

Table 1 Phase assemblages of reaction interfaces

Spot in Fig. 5	Content/wt.%				Content/at.%				Phase
	Ca	Si	Fe	Al	Ca	Si	Fe	Al	
a1	0.18	0.71	64.81	1.64	0.15	0.85	38.93	2.04	Wustite
a2	7.02	15.04	37.99	1.52	4.92	15.03	19.1	1.58	Residues
a3	12.23	11.27	38.6	1.3	8.78	11.54	19.89	1.38	AFMT
a4	4.78	1.1	59.24	0.4	3.83	1.25	34.03	0.47	FeO−CaO melt
a5	33.35	1.38	39.75	0.47	33.18	1.96	28.38	0.7	Calcium ferrite
b1	43.88	15.22	3.14	0.03	29.5	14.62	1.51	0.03	Ca_2SiO_4
b2	42.48	15.68	3.28	0.03	28.42	14.97	1.58	0.03	Ca_2SiO_4
b3	13.57	0.03	54.93	0.05	12.05	0.04	35.02	0.07	FeO−CaO melt
b4	28.82	1.14	37.86	0.4	23.29	1.31	21.96	0.48	Calcium ferrite
c1	46.81	16.04	1.31	0.02	28.53	13.95	0.57	0.02	Ca_2SiO_4
c2	46.68	15.99	1.28	0.03	28.57	13.96	0.56	0.03	Ca_2SiO_4
c3	30.8	0.77	36.07	0.78	22.68	0.81	19.06	0.85	Calcium ferrite
c4	7.52	0.01	63.27	0.02	6.86	0.01	41.4	0.03	FeO−CaO melt
d1	44.28	15.86	2.48	0.07	30.09	15.38	1.21	0.07	Ca_2SiO_4
d2	30.15	0.96	36.95	0.41	23.95	1.09	21.06	0.49	Calcium ferrite
d3	12.26	0.02	56.63	0	11.68	0.03	38.69	0	FeO−CaO melt
d4	46.88	10.26	3.9	0.06	32.46	10.13	1.94	0.06	Ca_3SiO_5
d5	46.67	10.53	3.76	0.06	32.38	10.44	1.86	0.06	Ca_3SiO_5
d6	44.53	15.57	2.48	0.07	30.22	15.09	1.2	0.07	Ca_2SiO_4
d7	44.28	15.69	2.5	0.07	30.17	15.28	1.21	0.07	Ca_2SiO_4

Spots designated by the letter prefixes a, b, c, and d correspond to Figs. 5(a), (b), (c), and (d), respectively

size, diffused more slowly compared to Ca^{2+} and Fe^{2+} [43,44], and its minimal diffusion concentration had no significant impact on the chemical reaction dynamics. Initially, the reaction primarily involved Ca^{2+} and Fe^{2+}, leading to the formation of calcium ferrite compounds and FeO−CaO melt. The calcium ferrite compounds were situated to the right of the cylindrical CaO, whereas the FeO−CaO melt was located to the left of the AFMT.

Increasing the temperature to 1300 °C and maintaining the reaction time at 1 s resulted in the formation of a Ca_2SiO_4 product layer at the FeO−CaO melt/AFMT interface, as shown in Fig. 7. This temperature rise enhanced the diffusion of SiO_4^{4-}. When the concentrations of SiO_4^{4-} and Ca^{2+} exceeded the solubility product of Ca_2SiO_4, precipitation occurred at the interface. The SiO_2−CaO system contains four compounds: $CaSiO_3$, $Ca_3Si_2O_7$, Ca_2SiO_4, and Ca_3SiO_5. Although the molar amount of CaO in the cylindrical CaO exceeded that of SiO_2 in the AFMT by more than threefold, the primary reaction product was Ca_2SiO_4, rather than Ca_3SiO_5. Such phenomena are also observed in industrial processes such as iron ore sintering, where the initial product with a CaO/SiO_2 molar ratio of approximately 1 is Ca_2SiO_4 rather than $CaSiO_3$. This can be attributed to the nonequilibrium nature of the decomposing reaction. Initially, the reaction is far from equilibrium, and the most stable compound, Ca_2SiO_4, precipitates as the primary product. At this juncture, at the FeO−CaO melt/AFMT interface, Ca_2SiO_4 precipitates abundantly, forming a Ca_2SiO_4 product layer. The increase in temperature facilitates mass transfer, thereby promoting the formation of the Ca_2SiO_4 product layer.

It is well-established that ion diffusion rates are significantly slower in the solid phase than in the melt. Therefore, further investigation of the

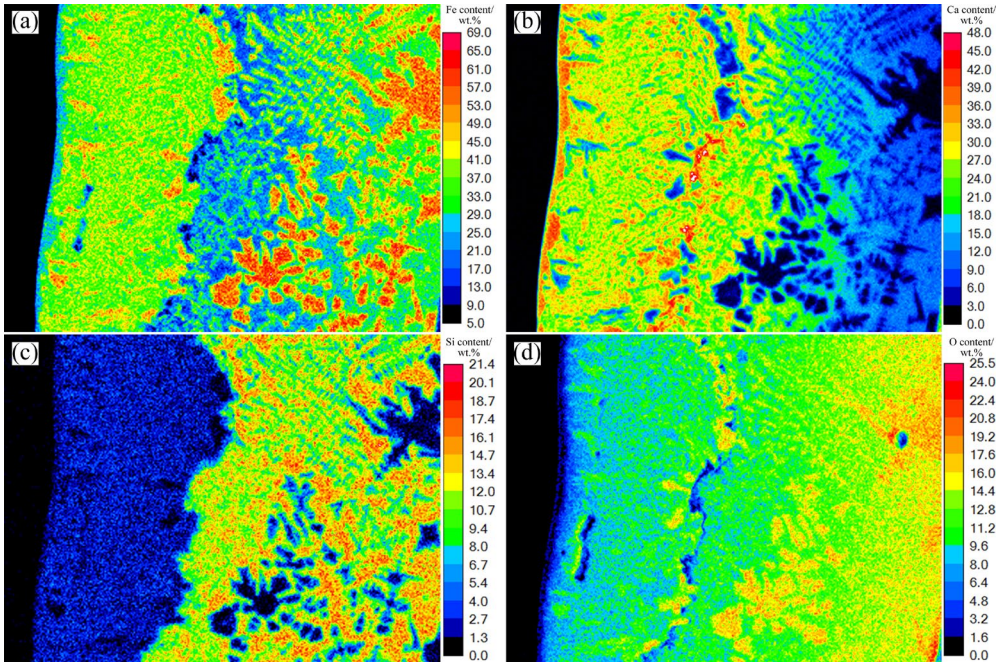

Fig. 6 Elemental distribution mappings at 1220 °C for 1 s: (a) Fe; (b) Ca; (c) Si; (d) O

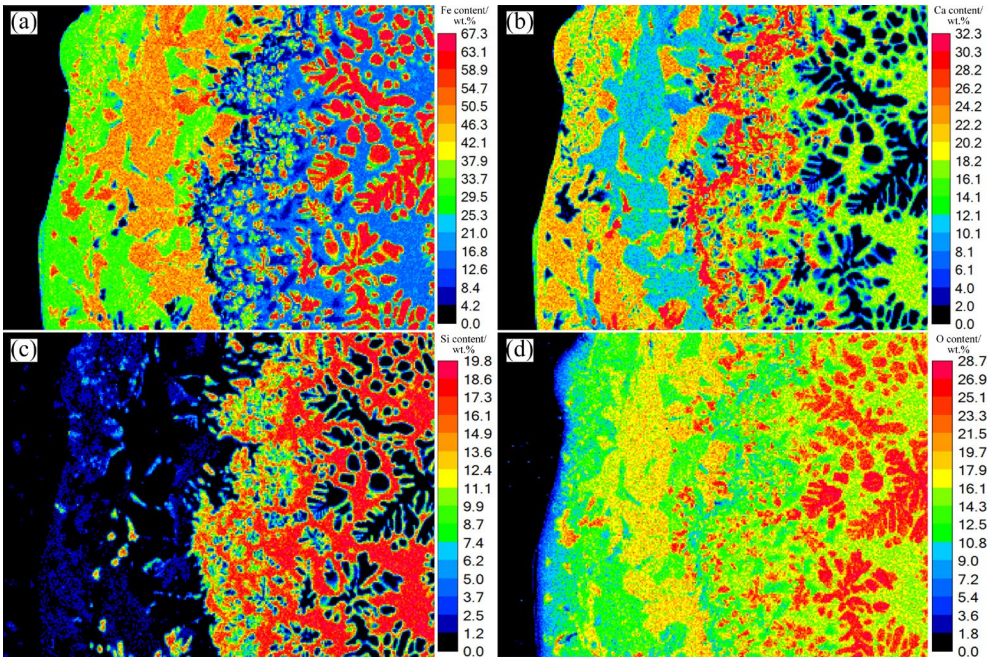

Fig. 7 Elemental distribution mappings at 1300 °C for 1 s: (a) Fe; (b) Ca; (c) Si; (d) O

potential impact of the Ca_2SiO_4 product layer, which spans between the CaO and the AFMT, on the chemical decomposition process is warranted.

4.2.3 Effect of time

Figures 5(b−d) illustrate the interfaces at 1300 °C for various reaction time, with the corresponding mapping images shown in Figs. 7−9. The Ca_2SiO_4 product layer visibly migrated to the right, incorporating several Ca_2SiO_4 particles within the coexistence zone of calcium ferrite compounds and FeO−CaO melt. By a reaction time of 30 s, these entrapped Ca_2SiO_4 particles were replaced by Ca_3SiO_5, and a small amount of Ca_2SiO_4 particles precipitated within the AFMT.

The formation of the Ca_2SiO_4 product layer significantly hindered the diffusion of Ca^{2+}, Fe^{2+}, and SiO_4^{4-}. The diffusion rates of Ca^{2+} and Fe^{2+} through the Ca_2SiO_4 layer were slowed down. SiO_4^{4-} was more severely affected, accumulating primarily to the right of the Ca_2SiO_4 layer and reacting with

diffused Ca^{2+}, leading to further precipitation of Ca_2SiO_4. On the opposite side of the Ca_2SiO_4 layer, the diffused Fe^{2+} initiated the dissolution of Ca_2SiO_4 and integrated into the coexistence zone of calcium ferrite compounds and FeO−CaO melt. Ca_2SiO_4 particles without being fully solubilized by Fe^{2+} were subsequently trapped within this zone. Over time, this cycle of formation and dissolution caused the Ca_2SiO_4 layer to shift noticeably to the right. Moreover, the thickness of the Ca_2SiO_4 layer depended on the different rates of its formation and dissolution.

As the reaction advanced, the Ca_2SiO_4 layer thickened and compacted, as depicted in Fig. 5(d). The diffusion rates of Ca^{2+} and Fe^{2+} through this layer were considerably reduced. SiO_4^{4-} failed to penetrate the Ca_2SiO_4 layer and was confined to homogenizing motion within the AFMT, as illustrated in Fig. 9(c). Only a limited amount of Ca^{2+} could diffuse through the Ca_2SiO_4 layer to interact with SiO_4^{4-} in the AFMT, severely restricting the precipitation of new Ca_2SiO_4 particles.

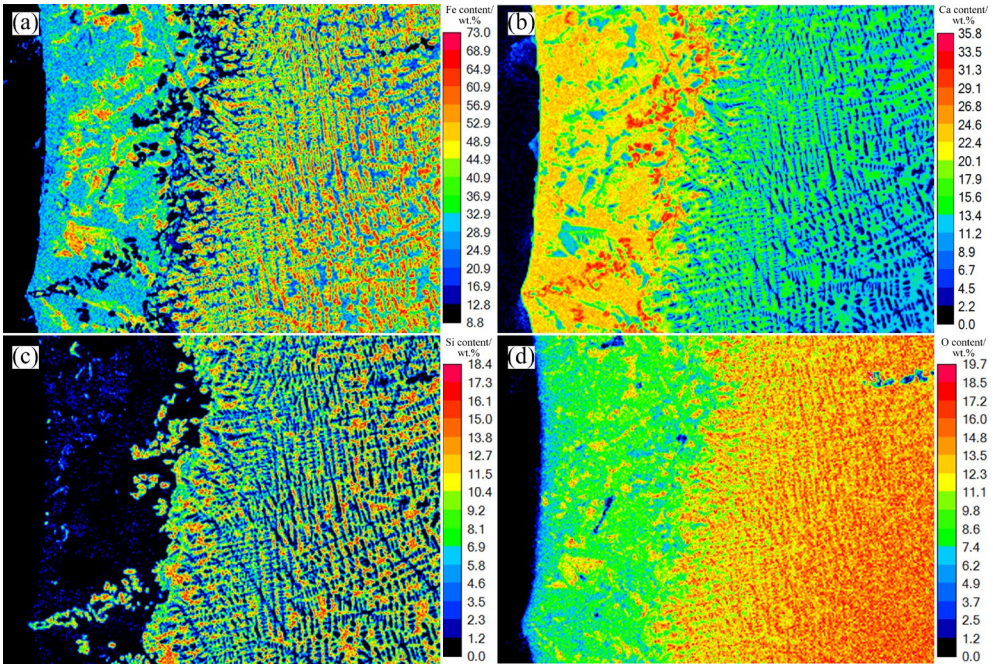

Fig. 8 Elemental distribution mappings at 1300 °C for 10 s: (a) Fe; (b) Ca; (c) Si; (d) O

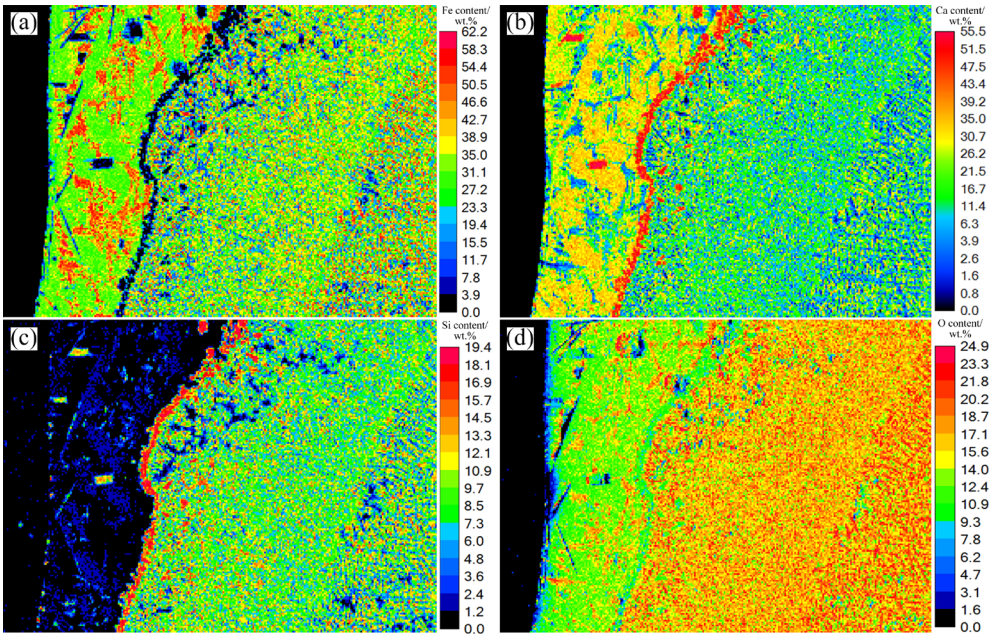

Fig. 9 Elemental distribution mappings at 1300 °C for 30 s: (a) Fe; (b) Ca; (c) Si; (d) O

Consequently, only a few Ca_2SiO_4 particles were observed in the bulk phase of the AFMT, with the residual FeO-enriched melt dispersed around them. To the left of the Ca_2SiO_4 layer, excessive Ca^{2+} within the coexistence zone initiated the conversion of entrapped Ca_2SiO_4 particles into Ca_3SiO_5.

In this study, the quantity of solid CaO exceeded three times that of the AFMT adhering to its surface. Thus, the chemical reaction involving CaO decomposing AFMT continued until all Ca_2SiO_4 was converted to Ca_3SiO_5.

4.2.4 Effect of Al_2O_3

Although Al_2O_3 was not directly involved in the formation of the main phases, as indicated in Table 1, its behavior warrants discussion. Figure 10 illustrates the distribution of Al at each reaction interface. Before the Ca_2SiO_4 product layer formed, the distribution of Al (Fig. 10(a)) resembled that of Si (Fig. 6(c)). As the experiments progressed, as depicted in Figs. 10(b) and (c), Al_2O_3 was observed to enrich on the right of the Ca_2SiO_4 layer. This enrichment faded as the Ca_2SiO_4 layer thickened and densified (Fig. 10(d)).

This enrichment of Al_2O_3 was closely related to the dynamics of the Ca_2SiO_4 layer. With the considerable precipitation of Ca_2SiO_4, the concentrations of SiO_4^{4-} and Ca^{2+} at the FeO−CaO melt/AFMT interface diminished rapidly, resulting in an increased Al_2O_3 concentration on the right of the Ca_2SiO_4 layer. Only a minimal amount of Al_2O_3 diffused through the Ca_2SiO_4 layer along with SiO_4^{4-}, dissolving into the calcium ferrite compounds. Initially, as the Ca_2SiO_4 layer formed, Al_2O_3 was enriched on its right. As the layer became more compact, Al_2O_3 diffusion was confined within the AFMT, resembling the behavior of SiO_4^{4-}, leading to a gradual decrease and eventual disappearance of the Al_2O_3 enrichment.

The impact of Al_2O_3 on the decomposition reaction is interesting. JIANG et al [37] explored the effects of Al_2O_3 on oxygen steelmaking slag and proposed that Al_2O_3 reacted with Ca_2SiO_4 to form $Ca_2Al_2SiO_7$. However, this compound was not detected in the current study. DEO et al [38] investigated the influence of Al_2O_3 on the morphology of oxygen steelmaking slag and noted that the presence of Al_2O_3 inhibited the formation of Ca_2SiO_4, reducing its quantity. The findings of this study corroborate this observation, as a reduced equilibrium concentration of FeO in residual melts implies suppressed precipitation of Ca_2SiO_4 particles. This conclusion is supported by applying the lever rule to the Ca_2SiO_4 primary phase field illustrated in Fig. 3. Moreover, the trace amounts of Al detected in Ca_2SiO_4 particles, as shown in Table 1, suggest the formation of an Al_2O_3-

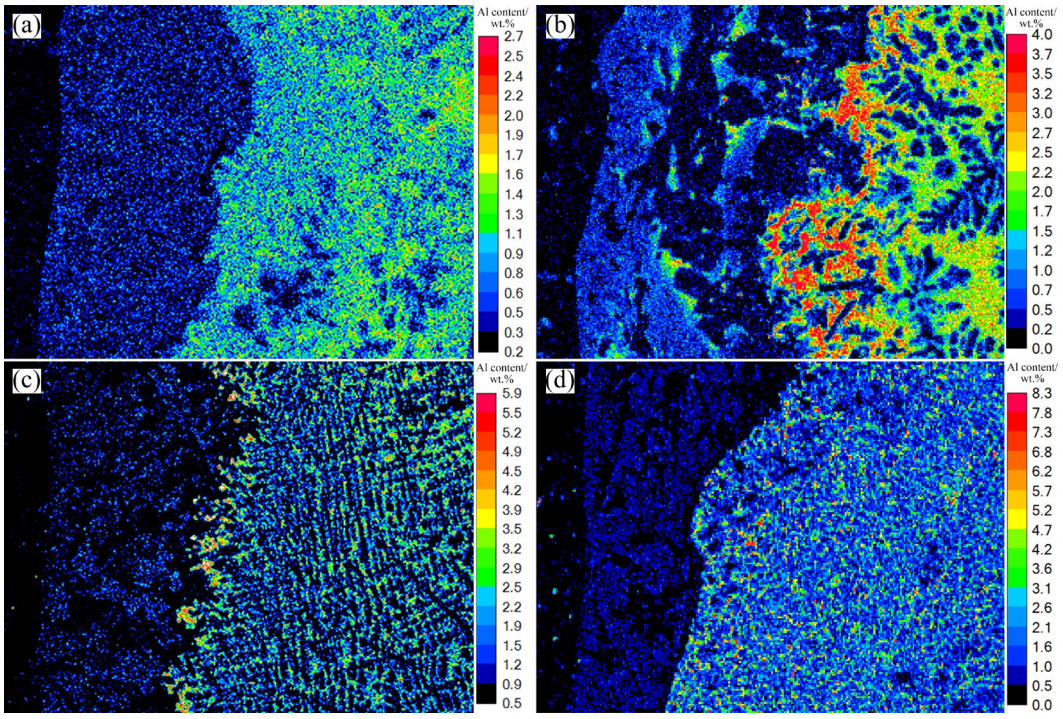

Fig. 10 Al distribution mappings at 1220 °C for 1 s (a), and at 1300 °C for 1 s (b), 10 s (c) and 30 s (d)

containing Ca_2SiO_4 solid solution, possibly through the partial substitution of SiO_4^{4-} tetrahedra by AlO_4^{5-} tetrahedra during the precipitation process.

4.3 Reaction mechanism

4.3.1 Retardation effect of Ca_2SiO_4 product layer

The widely recognized principle that ion diffusion rates are lower in solids than in melts provides a fundamental explanation for the retardation effect imposed by the Ca_2SiO_4 product layer on ion diffusion. The behavior of the initial products, the FeO−CaO melt and calcium ferrite compounds, offers deeper insights into this retardation phenomenon.

It was critical to determine the onset of this retardation effect, that is, the formation time of the Ca_2SiO_4 product layer. In Fig. 5(a), a considerable presence of FeO−CaO melt was noted, relative to the calcium ferrite compounds, with this disparity visibly diminishing in Fig. 5(b). Additionally, a comparison between Figs. 6(c) and 7(c) revealed a minor decrease in Si concentration as the temperature increased to 1300 °C, indicating a retardation in the relative diffusion of Ca^{2+}, Fe^{2+}, and SiO_4^{4-}. This effect could not be attributed solely to the rise in temperature. Instead, the formation of the Ca_2SiO_4 product layer seems the most plausible cause. Accumulation of Fe^{2+} and SiO_4^{4-} occurred on the right of the Ca_2SiO_4 layer, while Ca^{2+} accumulated on the left. These accumulations facilitated the observed alterations in the coexistence zone of calcium ferrite compounds and FeO−CaO melt. It can be inferred that the formation of the Ca_2SiO_4 product layer occurred earlier than the 1 s mark, as the retardation effect was already evident.

The impact of the Ca_2SiO_4 product layer on ion diffusion was further confirmed by examining the width of the coexistence zone between calcium ferrite compounds and FeO−CaO melt. As depicted in Fig. 11, the coexistence zone width was plotted against reaction time. This width was calculated as an average from measurements taken from the backscattered images in Figs. 5(b−d). The coexistence zone widths demonstrated average growth rates of 50, 4.4, and 0.5 μm/s during the intervals of 0−1, 1−10, and 10−30 s, respectively. These data confirm the significant retardation effect of the Ca_2SiO_4 layer on ion diffusion. Given that the formation of this layer occurred earlier than the 1 s mark, the retardation effect led to a pronounced reduction in the growth rate of the coexistence zone width. Furthermore, compared to Fig. 5(b), the proportion of FeO−CaO melt within the coexistence zone in Fig. 5(c) diminished and was replaced by calcium ferrite compounds. This, in turn, reinforced the retardation effect of the Ca_2SiO_4 product layer, as ions exhibit markedly slower mobility in solids than in melts. Table 1 indicated a decrease in Fe concentration and an increase in Ca concentration in the FeO−CaO melt as the interface reaction progressed from 10 to 30 s, supported by the elemental distributions in Figs. 8 and 9. This change was a direct result of the evolving retardation effect imposed by the Ca_2SiO_4 product layer.

HAMANO et al [35] observed that P_2O_5 in slag accelerates ion diffusion, thereby increasing the width of the coexistence zone, which was supported by HACHTEL et al [33] and KAKIMOTO et al [45]. SAITO et al [36] measured the coexistence zone width in CaO-decomposed P_2O_5-containing slag, as depicted in Fig. 11. The width reported in this study exceeds those noted by SAITO et al [36]. Although Al_2O_3 has a stronger accelerating effect on ion diffusion than P_2O_5, the impact of trace amounts of Al_2O_3 is insufficient to counterbalance the retardation effect of the Ca_2SiO_4 product layer on ion diffusion.

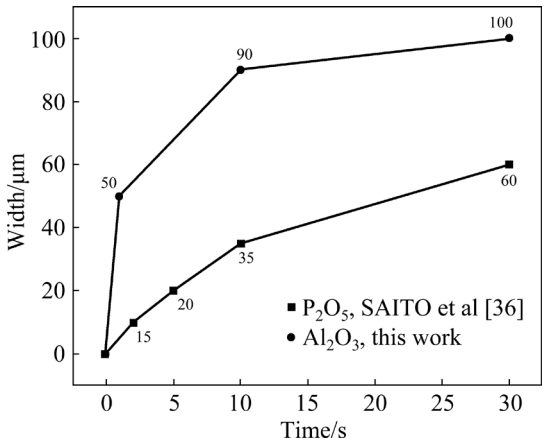

Fig. 11 Variation of coexistence zone width with time

In summary, the retardation effect of the Ca_2SiO_4 product layer on mass transfer is intensified over time, significantly reducing the rate of the decomposition reaction to near complete termination. The in-situ observations and quenching experiments in this study indicated that the system was far from reaching an equilibrium state. This

retardation effect also accounts for the near-constant reaction interface, as demonstrated in Fig. 4.

4.3.2 Self-retardation mechanism of lime decomposing AFMT

The equilibrium concentrations of species in a chemical system can be inferred from thermodynamic principles [46]. However, a broader experimental perspective is necessary to fully understand the specific reaction mechanisms. The results revealed that the dense Ca_2SiO_4 film formed by the target substance Ca_2SiO_4 severely impedes the mass transfer, demonstrating a self-retardation effect. This self-retardation mechanism, illustrated in Fig. 12, can be summarized as follows: (1) lime decomposing AFMT occurs through ion diffusion (Fig. 12(a)); (2) The initial reaction products include calcium ferrite compounds and FeO−CaO melt (Fig. 12(b)); (3) at the FeO−CaO melt/AFMT interface, Ca_2SiO_4 particles precipitate, forming a dense Ca_2SiO_4 film (Fig. 12(c)); (4) the diffusion rates of Fe^{2+} and Ca^{2+} through this dense Ca_2SiO_4 film are significantly reduced, and SiO_4^{4-} ions cannot penetrate the film (Fig. 12(d)); (5) although traces of Al_2O_3 can temporarily enhance mass transfer, they are insufficient to disrupt the structure of the dense Ca_2SiO_4 film. Within the coexistence zone of calcium ferrite compounds and FeO−CaO melt, an excess of Ca^{2+} facilitates the formation of Ca_3SiO_5. In the AFMT phase, the limited quantity of Ca^{2+} leads to the precipitation of only a few new Ca_2SiO_4 particles, with a minor amount of FeO-rich residual melt dispersing around them (Fig. 12(e)).

The dense Ca_2SiO_4 film poses a significant barrier to mass transfer, substantially extending the time to reach equilibrium for lime decomposing AFMT. Future research should therefore focus on modifying the structure and distribution of the Ca_2SiO_4 film to mitigate its retardation effects. Additionally, there has been some progress [47−49] in resolving the separation between Ca_2SiO_4 solid solution and FeO-rich melt. However, further development of alternative technologies suitable for industrial applications remains essential.

5 Conclusions

(1) According to the pseudo-ternary FeO−CaO−SiO_2 (Al_2O_3) system phase diagram, the regulation of CaO addition in the AFMT allows the production of residual melt with FeO concentrations of 75−88 wt.% and Ca_2SiO_4 at equilibrium. However, in-situ observations indicated that the reaction of lime decomposing AFMT was impacted by

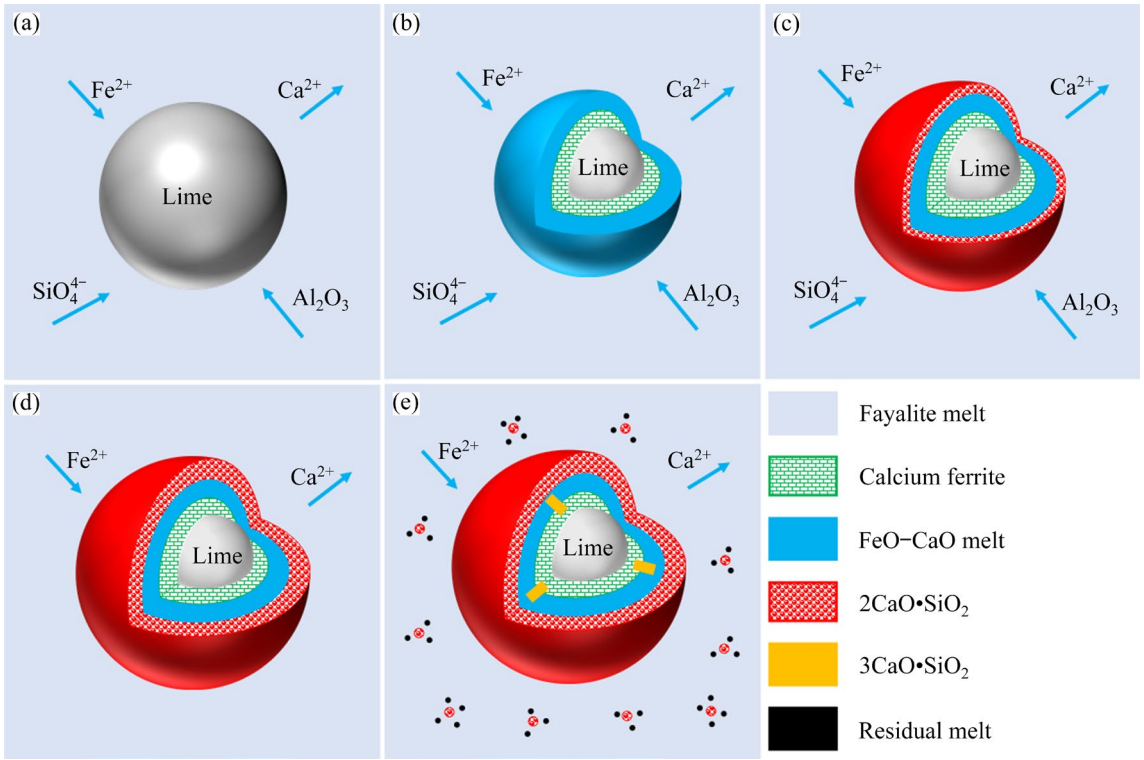

Fig. 12 Schematic diagrams of reaction mechanism for lime decomposing AFMT

unidentified factors, which significantly hindered its progression.

(2) The initial reaction products consisted of FeO−CaO melt and calcium ferrite compounds. At the FeO−CaO melt/AFMT interface, Ca_2SiO_4 particles precipitated, forming a dense Ca_2SiO_4 film that significantly retarded mass transfer. Although the temporary enrichment of Al_2O_3 due to the precipitation of Ca_2SiO_4 particles enhanced mass transfer, it was insufficient to overcome the retardation effect. The chemical reaction exhibited a self-retardation effect and was nearly terminated within the first 30 s, far from reaching an equilibrium state.

(3) It is recommended to use lime with sufficiently small particle size or porous characteristics or, alternatively, to employ strategies that modify the structure and dispersibility of the Ca_2SiO_4 film. Such approaches have the potential to mitigate the self-retardation effect, thereby enhancing the efficiency of the reaction kinetics.

CRediT authorship contribution statement

Hui-chuan REN: Conceptualization, Methodology, Investigation, Formal analysis; **Xiao-bo MIN:** Resources, Funding acquisition, Supervision; **Yong KE:** Formal analysis, Data curation, Project administration; **Long-gong XIA:** Writing – Review & editing; **Yun-yan WANG:** Formal analysis, Data curation; **Cong PENG:** Validation, Supervision, Project administration; **Yun LI:** Validation, Supervision; **Rong-he TAN:** Writing – Review & editing; **Chuan-fu ZHANG:** Validation, Supervision.

Declaration of competing interest

The authors declare that they have no known competing financial interests or personal relationships that could have appeared to influence the work reported in this paper.

Acknowledgments

This research was supported by the National Natural Science Foundation of China (No. 52121004), the National Science Fund for Distinguished Young Scholars (No. 51825403), the Science and Technology Innovation Program of Hunan Province, China (No. 2021RC3013), National Key R&D Program of China (No. 2022YFC3901602), and the Major Science and Technology Project of Gansu Province, China (No. 21ZD4GD033).

References

[1] PLÖTZ P, AXSEN J, FUNKE S A, GNANN T. Designing car bans for sustainable transportation [J]. Nature Sustainability, 2019, 2: 534−536.

[2] BENVENUTTI L M M, RIBEIRO A B, URIONA M. Long term diffusion dynamics of alternative fuel vehicles in Brazil [J]. Journal of Cleaner Production, 2017, 164: 1571−1585.

[3] KITO M, NAKAMOTO Y, KAGAWA S, HIENUKI S, HUBACEK K. Environmental consequences of Japan's ban on sale of new fossil fuel-powered passenger vehicles from 2035 [J]. Journal of Cleaner Production, 2024, 437: 140658.

[4] CHATTERJEE S, CHAUDHURI R, VRONTIS D, BRESCIANI S. Exploring the effect of government incentives on electric vehicle purchas intention in smart cities [J]. Journal of Cleaner Production, 2024, 477: 143841.

[5] ZHOU Xiang-yang, ZOU You-lan, ZHAO Guang-jin, YANG Juan. Cycle life prediction and match detection in retired electric vehicle batteries [J]. Transactions of Nonferrous Metals Society of China, 2013, 23: 3040−3045.

[6] SQUALLI J. Greening the roads: Assessing the role of electric and hybrid vehicles in curbing CO_2 emissions [J]. Journal of Cleaner Production, 2024, 434: 139908.

[7] LI Bai-hua, LI Hua-jiao, REN Shuai, LIU Hai-ping, WANG Gang. Commodity supply risk assessment of China's copper industrial chain: The perspective of trade network [J]. Resources Policy, 2023, 81: 103297.

[8] CHENG Xian-ming, YANG Ke, LIU Si-zhan, JI Shan-lin, WANG Jian. Microstructure and mechanical properties of ultrasonic welded copper to aluminum cables joints [J]. Transactions of Nonferrous Metals Society of China, 2023, 33: 3027−3038.

[9] KUMAR R, KHAN A A P, KHAN A, ASIRI A M, HAMID Y. Preparation and characterization of polyvinylchloride membrane embedded with Cu nanoparticles for electrochemical oxidation in direct methanol fuel cell [J]. Transactions of Nonferrous Metals Society of China, 2020, 30: 2207−2216.

[10] KLOSE S, PAULIUK S. Sector-level estimates for global future copper demand and the potential for resource efficiency [J]. Resources, Conservation and Recycling, 2023, 193: 106941.

[11] LI Ming-yang, ZHOU Shi-wei, LI Bo, WEI Yong-gang, WANG Hua. Migration of fluorine during the reduction of copper slag from spent cathode carbon produces copper−iron alloys [J]. Journal of Materials Research and Technology, 2023, 23: 1821−1833.

[12] WANG Kun, LIU Yan, HAO Jun, DOU Zhi-he, LV Guo-zhi, ZHANG Ting-an. A novel slag cleaning method to recover copper from molten copper converter slag [J]. Transactions of Nonferrous Metals Society of China, 2023, 33: 2511−2522.

[13] SARI Z A, TURAN M D. Investigation of atmospheric pressure leaching conditions and leaching kinetics in the obtaining of industrial copper(II) acetate solution from copper slags [J]. Journal of Central South University, 2023, 30: 2556−2573.

[14] ZHANG Hui-bin, WANG Ya-nan, ZHU Yin-bin, REN Peng, HU Bin, XU Sheng-hang, CAO Hua-zhen, ZHOU Jun, ZHENG Guo-qu. Determination of occurrence and leaching toxicity of arsenic in copper flash smelting slags [J]. Transactions of Nonferrous Metals Society of China, 2023, 33: 293−303.

[15] LI Qing-zhu, LI Ben-sheng, YAN Xue-lei, WANG Qing-wei, LI Sheng-tu, LIU Hui, LIANG Yan-jie. A review of arsenic reaction behavior in copper smelting process and its disposal techniques [J]. Journal of Central South University, 2023, 30: 2510−2541.

[16] WANG Da-wei, ZHAO Zong-wen, LIN Zhang, LIANG Yan-jie, KANG Li, PENG Bing. Interaction mechanism between arsenate and fayalite-type copper slag at high temperatures [J]. Transactions of Nonferrous Metals Society of China, 2022, 32: 709−720.

[17] TIAN Qing-hua, LI Zhong-chen, WANG Qin-meng, GUO Xue-yi. Synergistic recovery of copper, lead and zinc via sulfurization–reduction method from copper smelting slag [J]. Transactions of Nonferrous Metals Society of China, 2023, 33: 3847−3859.

[18] PIATAK N M, PARSONS M B, SEAL R R. Characteristics and environmental aspects of slag: A review [J]. Applied Geochemistry, 2015, 57: 236−266.

[19] LI Zhi, MA Guo-jun, ZHENG Ding-li, ZHANG Xiang, MUVUNYI R A. Effect of ZnO on the crystallization behavior and properties of SiO_2−CaO−Al_2O_3−Fe_2O_3 glass-ceramics prepared from simulated secondary slag after reduction of copper slag [J]. Ceramics International, 2022, 48: 21245−21257.

[20] GORAI B, JANA R K, PREMCHAND. Characteristics and utilisation of copper slag—A review [J]. Resources, Conservation and Recycling, 2003, 39: 299−313.

[21] PHIRI T C, SINGH P, NIKOLOSKI A N. The potential for copper slag waste as a resource for a circular economy: A review—Part I [J]. Minerals Engineering, 2021, 172: 107150.

[22] PHIRI T C, SINGH P, NIKOLOSKI A N. The potential for copper slag waste as a resource for a circular economy: A review—Part II [J]. Minerals Engineering, 2022, 180: 107474.

[23] FERNÁNDEZ-GONZÁLEZ D, RUIZ-BUSTINZA I, MOCHÓN J, GONZÁLEZ-GASCA C, VERDEJA L F. Iron ore sintering: Raw materials and granulation [J]. Mineral Processing and Extractive Metallurgy Review, 2017, 38: 36−46.

[24] POWNCEBY M I, CLOUT J M F. Importance of fine ore chemical composition and high temperature phase relations: Applications to iron ore sintering and pelletising [J]. Mineral Processing and Extractive Metallurgy, 2003, 112: 44−51.

[25] SRIVASTAVA U, KAWATRA S K. Strategies for processing low-grade iron ore minerals [J]. Mineral Processing and Extractive Metallurgy Review, 2009, 30: 361−371.

[26] LU Biao, WANG Suo-jin, TANG Kai, CHEN De-min. An all-factors analysis approach on energy consumption for the blast furnace iron making process in iron and steel industry [J]. Processes, 2019, 7: 607.

[27] NA Hong-ming, SUN Jing-chao, QIU Zi-yang, YUAN Yu-xing, DU Tao. Optimization of energy efficiency, energy consumption and CO_2 emission in typical iron and steel manufacturing process [J]. Energy, 2022, 257: 124822.

[28] FAN Y, SHIBATA E, IIZUKA A, NAKAMURA T. Crystallization behavior of copper smelter slag during molten oxidation [J]. Metallurgical and Materials Transactions B, 2015, 46: 2158−2164.

[29] FAN Y, SHIBATA E, IIZUKA A, NAKAMURA T. Crystallization behaviors of copper smelter slag studied using time−temperature−transformation diagram [J]. Materials Transactions, 2014, 55: 958−963.

[30] GYUROV S, KOSTOVA Y, KLITCHEVA G, ILINKINA A. Thermal decomposition of pyrometallurgical copper slag by oxidation in synthetic air [J]. Waste Management & Research, 2011, 29: 157−164.

[31] SELLEBY M. An assessment of the Ca−Fe−O−Si system [J]. Metallurgical and Materials Transactions B, 1997, 28: 577−596.

[32] DENG T, GRAN J, SICHEN D. Dissolution of lime in synthetic 'FeO'−SiO_2 and CaO−'FeO'−SiO_2 slags [J]. Steel Research International, 2010, 81: 347−355.

[33] HACHTEL L, FIX W, TRÖMEL G. Investigations into the dissolving of lime single-crystals in FeO_n−SiO_2 heats [J]. Archiv für das Eisenhüttenwesen, 1972, 43: 361−369. (in German)

[34] ZHONG L C, MUKAI K, ZEZE M, MIYAMOTO K ichiro, SANO N. In-situ observation of penetration of molten slag into solid lime at high temperature [J]. Steel Research International, 2007, 78: 236−240.

[35] HAMANO T, FUKAGAI S, TSUKIHASHI F. Reaction mechanism between solid CaO and FeO_x−CaO−SiO_2−P_2O_5 slag at 1573 K [J]. ISIJ International, 2006, 46: 490−495.

[36] SAITO R, MATSUURA H, NAKASE K, YANG X, TSUKIHASHI F. Microscopic formation mechanisms of P_2O_5-containing phase at the interface between solid CaO and molten slag [J]. Tetsu-to-Hagané, 2009, 95: 258−267. (in Japanese)

[37] JIANG Lu, DIAO Jiang, YAN Xiao-man, XIE Bing, REN Yi, ZHANG Tao, FAN Guo-zheng. Effect of Al_2O_3 on enrichment of phosphorus in hot metal dephosphorization slag [J]. ISIJ International, 2015, 55: 564−569.

[38] DEO B, HALDER J, SNOEIJER B, OVERBOSCH A, BOOM R. Effect of MgO and Al_2O_3 variations in oxygen steelmaking (BOF) slag on slag morphology and phosphorus distribution [J]. Ironmaking & Steelmaking, 2005, 32: 54−60.

[39] WANG Z J, SOHN I. A review of in situ observations of crystallization and growth in high temperature oxide melts [J]. JOM, 2018, 70: 1210−1219.

[40] JUNG S S, SOHN I. Crystallization behavior of the CaO−Al_2O_3−MgO system studied with a confocal laser scanning microscope [J]. Metallurgical and Materials Transactions B, 2012, 43: 1530−1539.

[41] BALE C W, CHARTRAND P, DEGTEROV S A, ERIKSSON G, HACK K, BEN MAHFOUD R, MELANÇON J, PELTON A D, PETERSEN S. FactSage thermochemical software and databases [J]. Calphad, 2002, 26: 189−228.

[42] KU Jiang-gang, ZHANG Lin, FU Weng, WANG Shu-bin,

YIN Wan-zhong, CHEN Hui-huang. Mechanistic study on calcium ion diffusion into fayalite: A step toward sustainable management of copper slag [J]. Journal of Hazardous Materials, 2021, 410: 124630.

[43] PARK J H, JUNG I H, LEE H G. Dissolution behavior of Al_2O_3 and MgO inclusions in the $CaO-Al_2O_3-SiO_2$ slags: Formation of ring-like structure of $MgAl_2O_4$ and Ca_2SiO_4 around MgO inclusions [J]. ISIJ International, 2006, 46: 1626−1634.

[44] OISHI Y, COOPER A R Jr, KINGERY W D. Dissolution in ceramic systems. III: Boundary layer concentration gradients [J]. Journal of the American Ceramic Society, 1965, 48: 88−95.

[45] KAKIMOTO S, KIYOSE A, MURAO R. Influence of P_2O_5 on dissolution behavior of lime in molten slag [J]. ISIJ International, 2017, 57: 1710−1717.

[46] BALE C W, BÉLISLE E, CHARTRAND P, DECTEROV S A, ERIKSSON G, GHERIBI A E, HACK K, JUNG I H, KANG Y B, MELANÇON J, PELTON A D, PETERSEN S, ROBELIN C, SANGSTER J, SPENCER P, ENDE M A. Reprint of: FactSage thermochemical software and databases, 2010—2016 [J]. Calphad, 2016, 55: 1−19.

[47] ONO H, INAGAKI A, MASUI T, NARITA H, NOSAKA S, MITSUO T, GOHDA S. Removal of phosphorus from LD converter slag by floating separation of dicalcium silicate during solidification [J]. Transactions of the Iron and Steel Institute of Japan, 1981, 21: 135−144.

[48] MIKI T, KANEKO S. Separation of FeO and P_2O_5 from steelmaking slag utilizing capillary action [J]. ISIJ International, 2015, 55: 142−148.

[49] LI Chong, GAO Jin-tao, GUO Zhan-cheng. Separation of phosphorus- and iron-enriched phase from $CaO-SiO_2-FeO-MgO-P_2O_5$ melt with super gravity [J]. Metallurgical and Materials Transactions B, 2016, 47: 1516−1519.

石灰分解含 Al_2O_3 铁橄榄石熔体的机理

任慧川[1]，闵小波[1,2,3]，柯 勇[1,2,3]，夏隆巩[1]，王云燕[1,2,3]，
彭 聪[1,2,3]，李 云[1,2,3]，谭荣和[4]，张传福[1,2,3]

1. 中南大学 冶金与环境学院，长沙 410083；
2. 有色金属强化冶金新技术全国重点实验室，长沙 410083；
3. 国家重金属污染防治工程技术研究中心，长沙 410083；
4. 长沙有色冶金设计研究院有限公司，长沙 410001

摘 要：提出利用石灰分解含 Al_2O_3 铁橄榄石熔体(AFMT)提高铜渣中铁品位的方法。热力学计算表明，调整 CaO/AFMT 的比例，可生成 FeO 质量分数为 75%~88%的残余熔体和 Ca_2SiO_4。原位观察表明，该反应受到某种阻碍。淬火实验表明，反应的初始产物为钙铁酸盐化合物和 FeO−CaO 熔体。在 FeO−CaO 熔体/AFMT 界面，Ca_2SiO_4 颗粒沉淀，形成一层致密的 Ca_2SiO_4 膜，严重阻碍了传质。虽然 AFMT 中微量的 Al_2O_3 暂时促进了传质，但不足以克服这种阻滞效应。分解反应远未达到平衡，表现出一种自阻滞效应。应采取措施消除这种自阻滞效应，提高反应动力学效率。

关键词：石灰；含 Al_2O_3 铁橄榄石熔体；Ca_2SiO_4 膜；自阻滞；传质

(Edited by Wei-ping CHEN)